Materials Advances

ROYAL SOCIETY OF CHEMISTRY

PAPER

View Article Online
View Journal | View Issue

Cite this: *Mater. Adv.*, 2024, 5, 1088

Bridging the gap: an in-depth comparison of CVT-grown layered transition metal dichalcogenides for supercapacitor applications†

Muhammad Habib, ‡*[a] Zahir Muhammad,‡[b] Yasir A. Haleem, *[c] Sajid Farooq,[d] Raziq Nawaz,[e] Adnan Khalil,[c] Fozia Shaheen,[f] Hamza Naeem,[g] Sami Ullah[h] and Rashid Khan*[i]

Layered transition metal dichalcogenides (TMDCs) have garnered immense interest in supercapacitor energy storage applications. Despite the growing reports on TMDCs in the context of electrochemical supercapacitor studies, the prevailing use of carbon-based additives often obscures their correct analysis and overshadows their intrinsic behavior. In this work, we meticulously analyzed supercapacitor characteristics of distinct TMDC materials without using carbon or any other conductive, revealing their pure intrinsic behavior, specifically focusing on highly crystalline 2H phase tantalum (Ta), tungsten (W) and zirconium (Zr)-based TMDCs, grown using the chemical vapor transport (CVT) technique. The grown materials were characterized using cutting-edge techniques like X-ray diffraction (XRD), Raman spectroscopy, and high-resolution transmission electron microscopy (HRTEM), ensuring a comprehensive perspective of the synthesized TMDCs. To delve into the electrochemical properties of the prepared electrodes, extensive analysis using cyclic voltammetry (CV), galvanostatic charge–discharge (GCD) and electrochemical impedance spectroscopy (EIS) was performed. The obtained results were further supported with density functional theory (DFT) calculations to get insights regarding the charge transfer mechanism and electronic density distribution proximate to the Fermi levels. The synergy between the experimental results and theoretical calculations significantly improved the validity of our findings, thus probing the comprehension and optimization avenues of TMDCs for superior supercapacitor performance.

Received 7th September 2023,
Accepted 11th December 2023

DOI: 10.1039/d3ma00672g

rsc.li/materials-advances

1 Introduction

Layered transition metal dichalcogenides (TMDCs) have attained so much consideration due to their diverse properties, which make them valuable materials for optical, electronic, and magnetic applications.[1–4] Qualitatively, TMDC crystals usually have highly pure, clearly defined crystal structures. The crystal growth parameters are critical and include growth rate, temperature, and pressure, *etc*. For high-quality crystals with consistent qualities, these parameters must be optimized. The electronic characteristics of these materials must be measured quantitatively in order to customize them for energy-related devices. The conductivity of TMDC crystals is largely determined by their electronic states. For electrical devices and energy storage systems to efficiently transmit charge, high charge carrier mobility is preferred. Comprehending and managing these characteristics is crucial for optimizing TMDC crystal performance in energy-related applications. TMDCs are also successfully applied as an active material in energy harvesting applications such as batteries, fuel cells and supercapacitors.[5–7] Among electrochemical energy storage devices, supercapacitors have emerged

[a] *Department of Physics, COMSATS University Islamabad, Lahore Campus, Lahore, Pakistan. E-mail: muhammad.habib@cuilahore.edu.pk*
[b] *Hefei Innovation Research Institute, School of Integrated Circuit Science & Engineering, Beihang University, Hefei 230013, P. R. China*
[c] *Institute of Physics, Khwaja Fareed University of Engineering & Information Technology, Rahim Yar Khan 64200, Pakistan. E-mail: yasir.haleem@kfueit.edu.pk, hiyasir@mail.ustc.edu.cn*
[d] *Centre for Lasers and Applications, Instituto de Pesquisas Energéticas e Nucleares, IPEN—CNEN, Sao Paulo 05508-000, Brazil*
[e] *CAS Key Laboratory of Ion-beam Engineering, Institute of Intelligent Machines, Hefei Institutes of Physical Science, Chinese Academy of Sciences, Hefei 230031, P. R. China*
[f] *Department of Physics, Government College (GC) University, Lahore 54000, Pakistan*
[g] *Department of Physics, Division of Science & Technology, University of Education, Lahore 54000, Pakistan*
[h] *K.A.CARE Energy Research & Innovation Centre (ERIC), King Fahd University of Petroleum & Minerals (KFUPM), Dhahran 31261, Saudi Arabia*
[i] *Zhejiang Provincial Key Laboratory of Advanced Chemical Engineering Manufacture Technology, College of Chemical and Biological Engineering, Zhejiang University, Hangzhou 310027, P. R. China. E-mail: rashid@mail.ustc.edu.cn*

† Electronic supplementary information (ESI) available. See DOI: https://doi.org/10.1039/d3ma00672g

‡ These authors contributed equally to this work.

with multiple intriguing characteristics of high-power density, stability, fast charging time and high capacitance values. There are abundant reports on electrochemical supercapacitor devices utilizing TMDCs as an active electrode material including their hybrids and composites with other materials.[8–10]

For supercapacitor measurements it has become a common trend to add conductive additives to the active electrode materials. Generally, carbon black,[11] conductive polymer,[12] acetylene black[13] and graphite[14] are used as an additive material and typically added in 7 to 10% of the total weight of the active electrode material. There are dedicated reports that have analysed the role of these additives and evaluated their performance.[15–17] These additives render overall improved device performance, thus increasing the stability and capacitance values manifold compared to the original value.[18–20] Besides improving performance, these additives may obscure intrinsic features and factual characteristics of the active electrode materials.

In this work, a comparative analysis was performed to reveal the intrinsic supercapacitor properties of tantalum, tungsten and zirconium-based 2H phase TMDC materials without using conductive additives. Six different TMDC materials, namely TaS_2, $TaSe_2$, WS_2, WSe_2, ZrS_2 and $ZrSe_2$, were synthesized and tested for electrochemical property studies without using conductive additives. Although TMDCs can be synthesized with CVD, hydrothermal, microwave-assisted or solution phase techniques,[21–24] we opted for the chemical vapor transport (CVT) technique due to its high purity crystalline nature yield.[25] The CVT technique is highly suitable for our work as it only requires distinctive constituent materials to grow a particular TMDC compound and does not require unnecessary precursors as in the case of other techniques. Other synthesis techniques may result in materials with impurity remnants, surface functional groups or defects[26,27] that make a profound contribution in determining the supercapacitor efficiency and obscure the original behaviour of the active electrode materials. This comparative analysis work may cast new insight into the fabrication and rational design of TMDC-based electrode materials.

2 Experimental

2.1 Transition metal dichalcogenide growth

For TMDC sample growth, research grade powder materials such as tantalum, tungsten, zirconium, sulphur and selenium were purchased from Sigma-Aldrich and used without applying further purification steps. For the sample preparation, stoichiometric amounts of the desired powders were mixed with 100 mg iodine as a transport agent. After thoroughly mixing, these materials were placed into a clean quartz tube. A quartz ampoule comprising 5 mm inner diameter and 25 cm length was used for growth purposes. Prior to use, ampoule tubes were thoroughly cleaned with diluted nitric acid and vacuum dried later. After putting powder materials in the clean tubes and right before sealing off, a vacuum of 10^{-3} torr was created in the tubes to get rid of air and to avoid oxidation of the sample during the growth process. Sealed tubes were carefully placed in a two-zone split-type heat furnace with the sample-containing side in a higher temperature zone, while the other side of the tube where crystals were to be grown was in a lower temperature zone. The growth temperatures for tantalum-based crystals (TaS_2 & $TaSe_2$) were 950 and 850 °C, for tungsten-based crystals (WS_2 & WSe_2) were 1030 and 930 °C and for zirconium-based crystals (ZrS_2 & $ZrSe_2$) were 950 and 850 °C for the sample and crystal growth zones, respectively. After cooling down of the furnace, the quartz ampoules were taken out and bulk form crystals were collected cautiously by breaking the ampoule. In order to get rid of any unreacted powder particles and iodine traces, the obtained materials were gently washed with acetone and isopropyl alcohol.

2.2 Electrode preparation and electrochemical measurements

The grown TMDC crystals were in a bulk form and could not be utilized directly for electrochemical measurements. For this purpose, crystals were thoroughly ground for about two hours to obtain the fine powdered form. For solution preparation, 2 mg of the ground powder was used in 750 μl DI water, 250 μl isopropyl alcohol and 10 μl Nafion was also added as a binding agent and the whole solution was sonicated for four hours. From the prepared solution, 5 μl solution was poured onto a glassy carbon electrode of 3 mm diameter and used for electrochemical measurements after drying at room temperature. Electrochemical measurements were taken at room temperature in 1 M H_2SO_4 electrolyte solution using a standard three-electrode configuration system. For measurements, a platinum mesh-shaped electrode was used as a counter electrode and Ag/AgCl (3 M KCl) was employed as a reference electrode.

2.3 Material characterizations and calculations

The crystallographic structures of the prepared transition metal dichalcogenides were studied with Panalytical X'Pert PRO MPD X-ray diffraction with Cu Kα radiation (λ = 1.54178 Å). Raman spectroscopy was performed with an XploRa ONE Raman microscope using a 532 nm laser and structural morphology was analysed with HRTEM images obtained using JEOL JEM2010. All electrochemical measurements were accomplished with a 600E potentiostat electrochemical analyser by CH Instruments. All Density Functional Theory (DFT) results were derived by employing the Vienna Ab initio Simulation Package (VASP) code.[1–3] The exchange–correlation functional[4] by using the General Gradient Approximation (GGA) of Perdew–Burke–Ernzerhof (PBE)[5] with the Projector Augmented Wave (PAW) technique[6,7] was used to generate all the DFT results while taking into account spin polarization. The six compounds, TaS_2, $TaSe_2$, WS_2, WSe_2, ZrS_2 and $ZrSe_2$ were formed by combining transition metals (Ta, W and Zr) and chalcogens (S and Se). The applied PAW–PBE pseudopotentials were selected according to the valence electrons (*i.e.*, Ta & W: 5p6s5d, Zr: 4s4p5s4d and S & Se: 2s4p) and a suitable cutoff energy was set for each compound. The cutoff energy of 520 eV for the plane wave basis set, the force convergence of 0.01 eV $Å^{-1}$, and the energy convergence criterion of 10^{-6} eV

were used. The Brillouin-zone was modelled by 7 × 7 × 1 Monkhorst–Pack *k*-points for sufficient geometric optimization and total energy calculation. The recommended *Γ*-centred grid for the hexagonal phase with an appropriate *k*-points set and an accurate condition of forces (below 0.0001 > eV) are used for structural relaxation. As a pseudopotential method, the effective core potentials, in which some degree of relativistic corrections were introduced into the core electrons, were employed.

3 Results and discussion

The optical images of the CVT synthesized crystals are shown in Fig. 1(a). It can be noticed distinctly that the synthesized crystals exhibit random shapes within the millimetre scale. X-ray diffraction patterns of the CVT grown TMDCs are shown in Fig. 1(b). It can be observed that all TMDC materials showed narrow and sharp peaks, which is evidence of high-quality crystal growth. High intensity sharp peaks, observed in the range around 13 to 16°, reveal the layered growth of our samples, which is a typical feature of transition metal dichalcogenide materials. In the XRD profiles of TaS_2 and $TaSe_2$, major peaks were found at ∼14.8 and ∼13.8° which referred to the (001) and (004) planes, respectively. The peaks at around 35 and 46.6° were well matched with the (101) and (1010) peaks of TaS_2 and $TaSe_2$, respectively. In the case of WS_2 and WSe_2, it can be seen that major peaks appeared at around 14.3 and 13.7°, which corresponded to the (002) peaks. Similarly, the peaks observed at ∼39.5 and ∼37.8° were ascribed as (103) peaks of both materials. Likewise, two intense peaks at around 15 and 14.4° can be stated as (001) peaks of the XRD profiles of ZrS_2 and $ZrSe_2$, respectively, while at ∼34°, the (101) peak of ZrS_2 at around 31°, and (102) peak of $ZrSe_2$ were identified. X-ray diffraction peak analysis confirms the hexagonal crystallographic structure of the CVT-synthesized TMDC samples. It was further investigated that the synthesized TaS_2 and $TaSe_2$ matched with the JCPDS card numbers 02-0137 and 21-1200, and WS_2 and WSe_2 with 08-0237 and 38-1388, while ZrS_2 and $ZrSe_2$ with 11-0679 and 03-065-3376, respectively.

The structure of the synthesized materials was further analysed by means of their vibrational modes using Raman spectroscopy given in Fig. 2. The Raman spectra of TaS_2 exhibited one in-plane vibrational mode E_{2a} (or represented

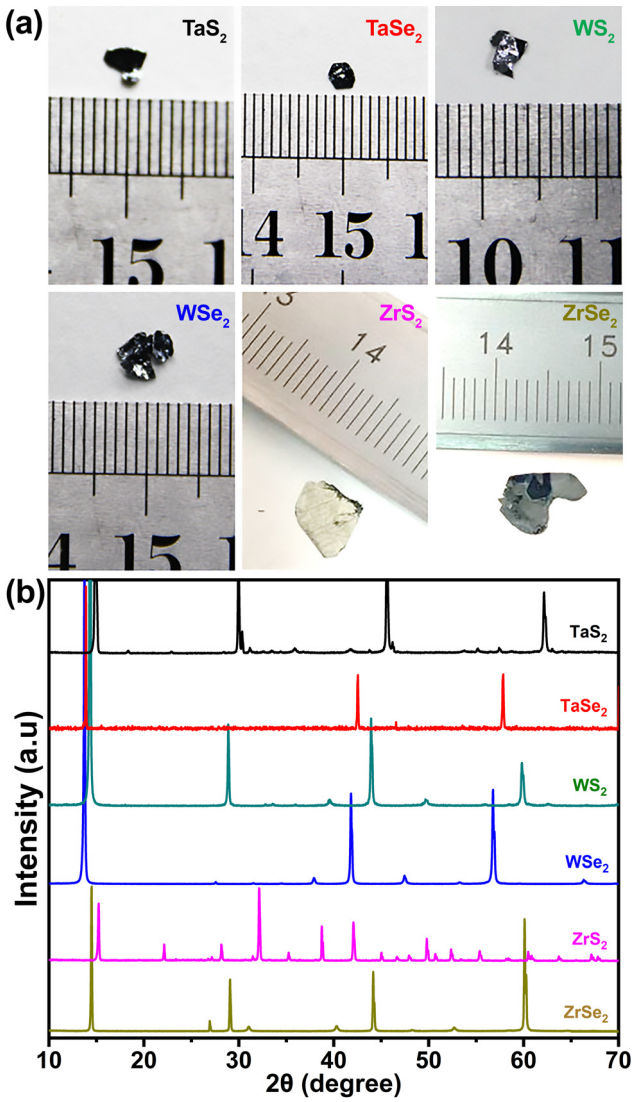

Fig. 1 (a) Optical images and (b) X-ray diffraction patterns of the grown transition metal dichalcogenides.

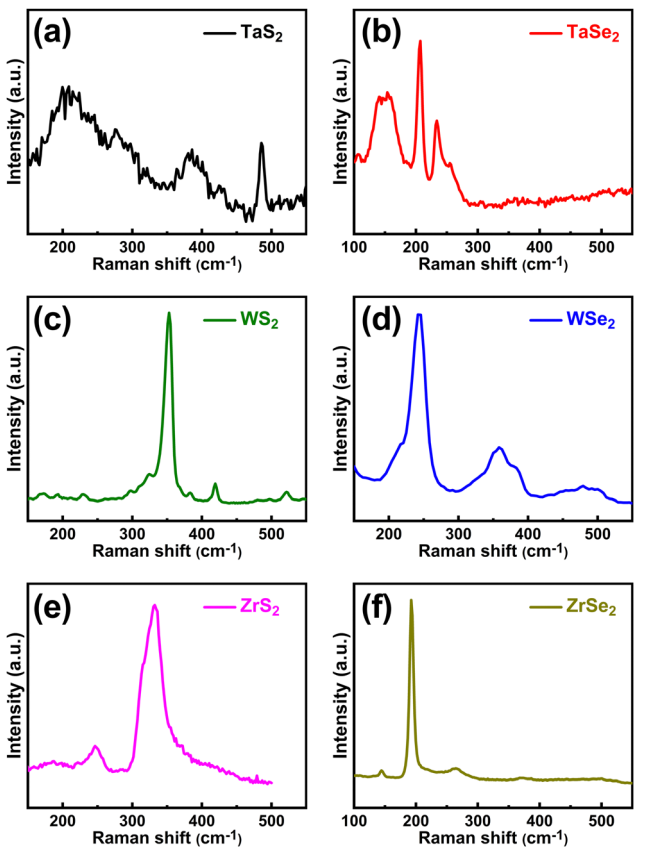

Fig. 2 Raman spectra of the CVT grown TMDCs. (a) TaS_2 and (b) $TaSe_2$, (c) WS_2 and (d) WSe_2, (e) ZrS_2 and (f) $ZrSe_2$.

by E^1_{2a} as in ref. 28) at ~280 cm^{-1} and one out-of-plane mode A_{1g} at ~388 cm^{-1}. The broader peak that appeared at around 212 cm^{-1} is attributed to the second order scattering. Similarly, three peaks were observed in the $TaSe_2$ measured spectra at ~148, 206 and 236 cm^{-1} which correspond to E_{1a}, E^1_{2a} and A_{1a} modes, respectively. The measured Raman modes for TaS_2 and $TaSe_2$ are in good agreement with the reported work.[29,30] In the WS_2 spectra, two peaks appeared at ~354 and ~422 cm^{-1} that correspond to E^1_{2a} and A_{1a} modes, respectively, whereas one peak was observed in the WSe_2 spectra at ~245 cm^{-1} which matches with its standard E^1_{2a} in-plane vibrational mode.[31] In the case of ZrS_2, the observed peaks were ascribed to E_g (in-plane) and A_{1g} (out-of-plane) vibrational modes that appeared at ~247.5 and ~333.5 cm^{-1} respectively. Correspondingly, in the $ZrSe_2$ Raman curve, one major peak was found at ~193 cm^{-1} which was attributed to A_{1g} and a small peak appeared at ~144 cm^{-1} associated with the E_g vibrational mode. Another small peak was seen at ~263 cm^{-1} that possibly appeared due to the density of the two phonon states.[32] The observed peaks and corresponding values in the spectra matched well with the reported literature.[33,34]

Fig. 3 shows the high-resolution transmission electron microscopy (HRTEM) images of the synthesized TMDCs. The results (Fig. 3(a)–(f)) reveal that bulk TMDC materials were grown in multiple layer stacking. The measured layer spacing for all TMDC materials was determined with their corresponding XRD peaks found at around 13 to 16°. In more detail, the (001) and (004) planes of the TaS_2 and $TaSe_2$ XRD data were closely matched with the HRTEM measured ~0.602 and ~0.636 nm interlayer spacings of these materials. Similarly, the assessed layer spacings of 0.618 nm for WS_2 and 0.638 nm for WSe_2 corresponded to the (002) peak of their XRD data. For ZrS_2 and $ZrSe_2$, using HRTEM, the interlayer spacings appeared to be 0.661 and 0.668 nm, which can be referred to their (001) XRD peak. Correspondingly, lattice plane spacings were also marked according to their matched X-ray diffraction peaks. The appeared (101) and (1010) XRD peaks of TaS_2 and $TaSe_2$ correspond to their lattice spacings of around 0.264 and 0.191 nm, respectively. Similarly, the ~0.231 and ~0.228 nm plane spacings of WS_2 and WSe_2 matched with the (103) peak. Relatedly, the plane spacings of the ZrS_2 and $ZrSe_2$ electrode materials can be referred to their (101) and (102) peaks. Dissimilar inter-layer spacing values observed in the HRTEM images are obvious due to the different atomic radii of the various transition metals and chalcogens used in this study. The obtained HRTEM images clearly revealed the layered structures and high crystalline quality of the grown TMDC materials. The layered structure of these materials is one of the key factors to determine their supercapacitive performance. Wider layer spacing is favourable for the ions to interact and swiftly flow through these layers, which will consequently increase the specific capacitance. On the other hand, narrower layer spacing restricts the flow of ions, which results in the reduction of the performance.

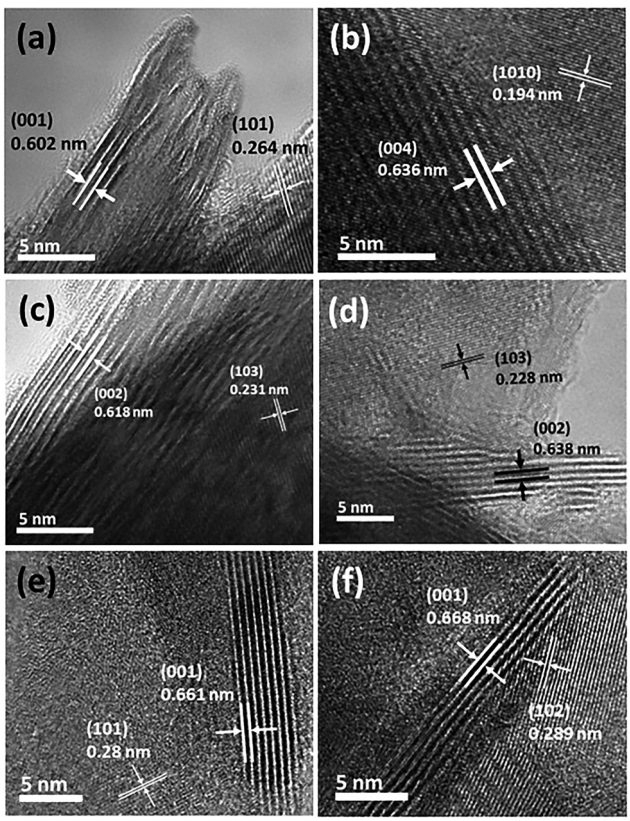

Fig. 3 High resolution TEM images showing layer and plane spacings of the CVT grown TMDCs. (a) TaS_2 and (b) $TaSe_2$, (c) WS_2 and (d) WSe_2, (e) ZrS_2 and (f) $ZrSe_2$.

Cyclic voltammogram (CV) curves, drawn from 0 to 0.5 V potential range at 100 mV s^{-1} scan rate, for all six electrode materials are shown in Fig. 4(a) while Fig. 4(b) illustrates the galvanostatic charge–discharge (GCD) curves, taken at a current density of 0.3 A g^{-1}. Specific capacitance values for the prepared electrode materials were calculated with the GCD curves by using the formula given in eqn (1).[35]

$$C = I\Delta t/A\Delta V \quad (1)$$

where C is the specific capacitance of the electrode materials, I and Δt are the discharge current and discharge time, A is the area of the electrode and ΔV represents the potential (after IR drop) of the GCD measurements.

The calculated specific capacitance values for TaS_2, $TaSe_2$, WS_2, WSe_2, ZrS_2 and $ZrSe_2$ were 151.11, 102.6, 116.1, 152.3, 141.8 and 127.3 F cm^{-2}, respectively. The comparison of the calculated gravimetric specific capacitances from both CV and GCD is given in Table S1 of the ESI.† All CVT grown samples were electrochemical double-layer capacitor (EDLC) type with nearly rectangular shapes and the absence of redox peaks in the CV curves.[36,37] Similar non-faradaic observations were witnessed in the charge–discharge curves as well. It is most probable that faradaic reactions occur at low scan rates and current densities. Therefore, to further affirm the nature of the prepared electrode materials CV curves at the low and higher scan rates of 5, 10, 20 and 40 mV s^{-1} were conducted, which are given in Fig. S1 in the ESI.† Similarly charge–discharge

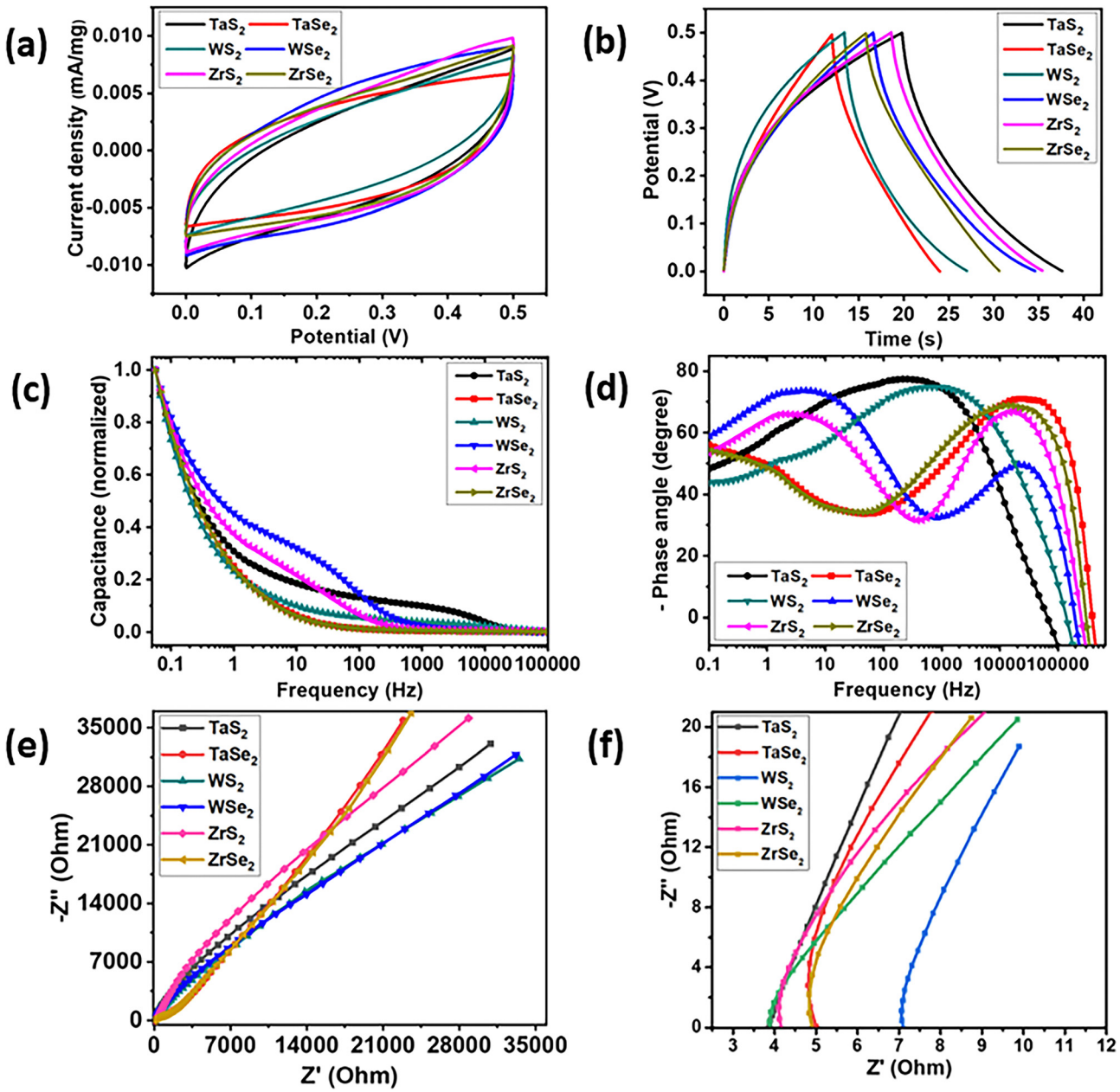

Fig. 4 (a) Cyclic voltammetry, (b) galvanostatic charge–discharge; Bode plots of (c) capacitance-frequency and (d) phase angle-frequency; (e) Nyquist plots of electrochemical impedance spectroscopy and (f) magnified plots at higher frequencies.

measurements, performed at 0.2, 0.4 and 0.5 A g^{-1} current densities, are also provided in Fig. S2 of the ESI.† The nonappearance of redox peaks, particularly in the low scan rate CV curves, and the absence of any plateau in the GCD curves are manifestations of EDLC behaviour. These observations are reflected in the measurements due to the absence of functional groups at the surface of the electrode materials. The exhibition of double layer (EDLC) supercapacitor behaviour by transition metal dichalcogenides is already reported in the literature.[21,38,39]

Fig. 4(c) represents a plot where the trend of the electrode's capacitance (normalized) against a range of frequencies can be found. It can be observed that the WSe_2 electrode possessed the highest capacitance value followed by ZrS_2 up to around 500 Hz. On the contrary, although the TaS_2 electrode encompasses relatively less capacitance, it holds it for a wide frequency range that is ~15 kHz. Other electrodes demonstrated almost a similar trend of capacitance *versus* frequency range. A typical supercapacitor (SC) device features its nature at low frequencies and resistive behaviour at higher frequencies, which are measured in the form of Bode plots.[40] Fig. 4(d) illustrates phase angle *versus* frequency Bode plots of the prepared electrode that were calculated using eqn (2).[41]

$$C = -1/2\pi f Z'' \quad (2)$$

where C, f and Z'' are the calculated capacitance, frequency and imaginary part of the impedance. It can be observed in the plots

that the WSe_2 and ZrS_2 electrodes manifested a better supercapacitor nature with higher phase angle values of around 75° and 65°, respectively, at low frequency ranges and then made transition into resistive mode at ~700 and ~300 Hz, respectively. Bode plots further revealed that the TaS_2 electrode showed the highest phase angle of 77° by covering a broader frequency range of up to around 3 kHz. The analysis further unveiled that the WS_2 electrode initially displays low phase angle values in the lower frequency region but attains a relatively high value of 75° at around 1 kHz and sustains its supercapacitor feature up to ~10 kHz. $TaSe_2$ and $ZrSe_2$ electrodes displayed almost similar characteristics with starting phase angle values of ~55° in the low frequency region (0.1 to 1.5 Hz) and shifted to the resistive region of operation after 10 Hz.

The Nyquist plot of electrochemical impedance spectroscopy (EIS) is another tool to analyse the intrinsic characteristics of the synthesized electrode materials. EIS was performed in a frequency range of 0.01 Hz to 1 MHz with a 0.005 (system generated) AC voltage signal. The higher straight line in the low frequency region corresponds to Warburg impedance and reflects the ideal supercapacitor behavior.[42,43] From the Nyquist plots of Fig. 4(e), it can be observed that the $TaSe_2$ and $ZrSe_2$ electrodes showed higher straight lines at low frequencies that eventually lessened while moving towards the higher frequency region. The TaS_2 electrode, which showed a high phase angle at relatively higher frequencies, can also be differentiated in the EIS graphs with its high slope even after the mid frequency region. Fig. 4(f) represents the higher frequency region, which highlighted the x-axis (Z') intercepts of the EIS curves to determine the interface resistance (R_s) of the corresponding electrode materials. It is clear from the Z' intercept that TaS_2 and WSe_2 materials showed similar interface resistance values of 3.8 Ohm followed by a comparable value of 4.1 Ohm for the ZrS_2. The WS_2 electrode showed a relatively high interface resistance value of ~7.1 Ohm among all electrode materials. To further reveal the conductivity and to determine the contribution of the charge transfer resistance (R_{ct}) in our electrode materials, we have plotted individual impedance spectroscopy graphs in Fig. S3 of the ESI.† EIS plots are also supplemented with the inset circuit models constructed after EIS curve fitting. From the fitted data values, it was observed that the TaS_2, WSe_2 and ZrS_2 electrodes showed low resistance values of around 32, 50 and 175 Ohm, respectively, as compared to 300, 238 and 530 Ohm for the $TaSe_2$, WS_2 and $ZrSe_2$ electrodes, respectively. The interface resistance values obtained from the simulated curves are comparable to the values obtained at the high frequency region of the Nyquist plots. The EIS findings are further verified with the density of states calculations in the coming discussions.

Stability is an essential parameter of a supercapacitor which was conducted for 5000 charge–discharge cycles at 0.3 A g^{-1} current density for each electrode. In terms of capacitance retention, curves illustrating the stability of the individual electrode material are shown in Fig. 5(a)–(f). Some of the highest capacitance retention of about 98% was displayed by the WS_2, WSe_2, and $TaSe_2$ electrodes. They were followed by Zr-based electrode overlapping curves that experienced about 8% loss in capacitance, while the TaS_2 electrode showed around 19% capacitance loss. To elaborate a comparative view, combined stability curves for all electrodes are given in Fig. S4 of the ESI.† Careful analysis of the prepared materials revealed that almost all electrode materials exhibited stable supercapacitor features due to the least defects and highly crystalline nature obtained from the adopted chemical vapor transport technique. It can be interpreted that a loss in capacitance occurred for the first couple of hundred cycles and then the electrode materials possess very stable features up to the rest of the 5000 cycles. The early decrease in capacitance retention is attributed to the preliminary time taken by the system to get electrochemically stabilized. The initial capacitance reduction in the stability is due to the feeble interactions between the electrolyte and active electrode material and saturation of active sites. A similar trend of initial capacitance reduction was also observed in the previously published works.[39,44,45]

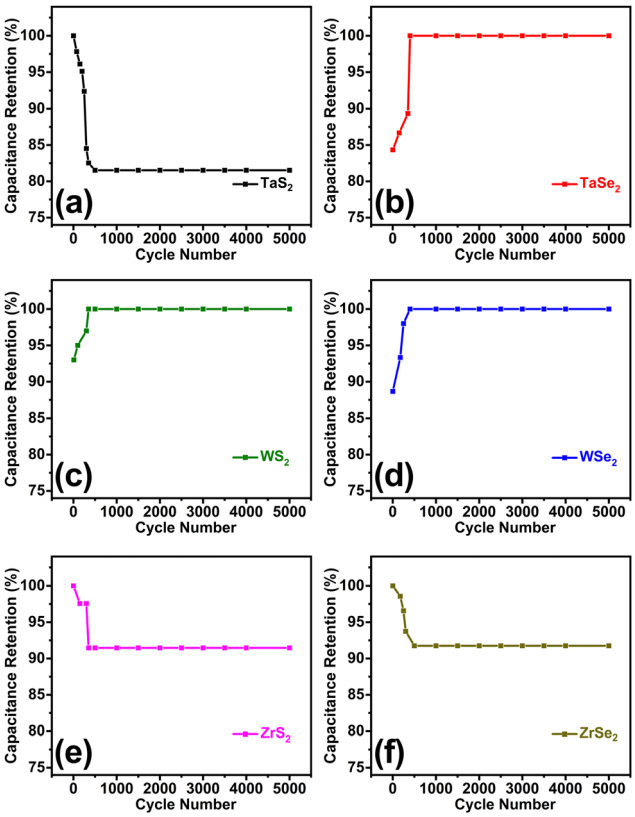

Fig. 5 Stability curves of (a) TaS_2, (b) $TaSe_2$, (c) WS_2, (d) WSe_2, (e) ZrS_2 and (f) $ZrSe_2$ electrodes measured for the first 5000 cycles.

Understanding how conductivity and electrochemical performance interplay is essential to comprehending material behaviour, especially in the context of devices like supercapacitors. As semiconductors, TMDCs have the capacity to contribute electrons to the conduction band and this capability has a direct impact on their conductivity. When TMDCs have high conductivity, they can readily donate or accept charges during electrochemical reactions. This ability is particularly important for the overall efficiency of the electrochemical processes

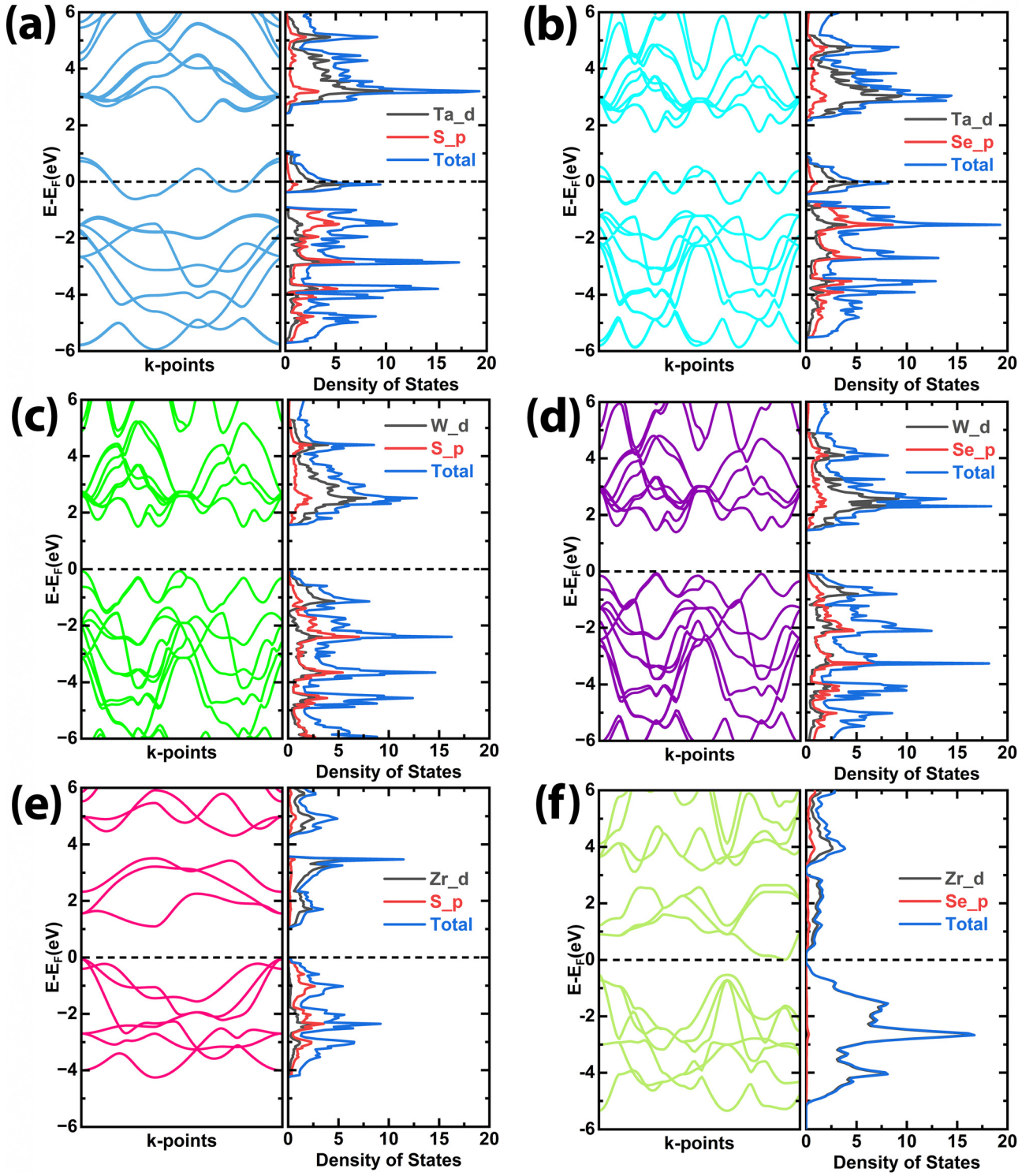

Fig. 6 Calculated band structure and partial density of states (PDOS) of (a) TaS_2, (b) $TaSe_2$, (c) WS_2, (d) WSe_2, (e) ZrS_2, and (f) $ZrSe_2$, respectively.

occurring in the device. The electronic band structure and partial density of states (PDOS) were calculated for all the structures to see the contribution of orbitals in the conduction and valence band in the electronic structure of these materials and their conductivity related to the bandgaps is shown in Fig. 6. The electrochemical performance of these materials depends on the electronegativity of the anion and cation atoms that contributed near the Fermi level in the d-orbitals. Fig. 6(a) and (b) show the band structure and PDOS of TaS_2 and $TaSe_2$, respectively. It can be seen that for TaS_2 the conduction band crossed the Fermi level, which belongs to Ta-d orbitals, while from the PDOS it is also observed that below the Fermi level the

Table 1 A comparison of our work with previously published studies on 2D materials

S. no.	Material	Binder	Additive	No. of cycles	Capacitance retention (%)	Ref.
1	TaS_2	Nafion	None	5000	81	This work
2	$TaSe_2$	Nafion	None	5000	98	This work
3	WS_2	Nafion	None	5000	98	This work
4	WSe_2	Nafion	None	5000	98	This work
5	ZrS_2	Nafion	None	5000	92	This work
6	$ZrSe_2$	Nafion	None	5000	92	This work
7	Ti_2C	PTFE	Conductive carbon	6000	93	Rakhi *et al.*[52]
8	Ti_3C_2	PVDF	Acetylene black	6000	88	Cao *et al.*[53]
9	Nb_2C	PVDF	Acetylene black	10 000	81	Ayesha *et al.*[54]
10	V_2C	PTFE	Carbon black	10 000	90	Yunfeng *et al.*[55]
11	V_2N	PVDF	Carbon black	10 000	96	Sandhya *et al.*[56]
12	MoS_2	PVDF	Carbon black	1000	70	Gupta *et al.*[57]
13	MnO_2 (nanoflake)	PVDF	Carbon black	1000	50	Sagar *et al.*[58]
14	RGO@Cuf	None	None	5000	92	Taniya *et al.*[59]

maximum density of states appeared contributed by the Ta-d orbital. The PDOS also further crossed the Fermi level and enhanced the conductivity of the TaS_2. Whereas, for $TaSe_2$ (Fig. 6(b)) the conduction band also crossed the Fermi level, however, the uneven distribution of PDOS is less deep in the conduction band than TaS_2 (see Fig. 6(a)). This could be the reason for the better electrochemical properties of TaS_2. Fig. 6(c) and (d) show the band structure and PDOS of WS_2 and WSe_2. Compared to WS_2 (see Fig. 6(c)), the WSe_2 has a lower energy gap (see Fig. 6(d)); therefore, WSe_2 has better conductivity. Meanwhile, the PDOS distributions in the valence bands are closer to the Fermi level, with strong hybridization of the W-d orbitals near the Fermi level. Therefore, due to the smaller band gap energy and strong hybridization of the W-d orbitals adjacent to the Fermi level, the transfer of charge is easier in the case of WSe_2, which causes better electrochemical performance. Similarly, Fig. 6(e) and (f) shows the band structure and PDOS of ZrS_2 and $ZrSe_2$, respectively. From the band structure of $ZrSe_2$, it is shown that the valence band is closer to the Fermi level for ZrS_2 as compared to $ZrSe_2$, which reveals that the transfer of charge is much stronger for ZrS_2. At the same time, it can also be seen that the PDOS near the Fermi level in ZrS_2 is much higher as compared to $ZrSe_2$, which makes ZrS_2 a better conductive material than $ZrSe_2$, having better performance for electrochemical properties. From these results, it is determined that the energy gap and carrier concentration near the Fermi level have a major role in the electronic conductivity of these TMDCs, which enhances the electrochemical performance of these materials due to the charge transfer mechanism.

The materials with higher carrier concentration near the Fermi level are more appropriate to donate electrons or holes to the conduction band, which increases their conductivity and hence increases the electrochemical performance. Our calculation results are in agreement with the experimentally obtained EIS results and the predicted higher (comparative) conductivities of the TaS_2, WSe_2 and ZrS_2 are verified with the charge transfer resistance value trend found from the EIS results. It is further mentioned that the performance of any electrode material is markedly influenced by factors like conductivity,[46] surface area,[47] electrolyte-type,[48,49] defects[50] and surface functional groups.[51] In addition, we have made a comparison between our results and the previously published literature that focuses primarily on 2D materials; this comparison is shown in Table 1.

The comparison clearly shows that the intrinsic performance of TMDC electrodes without additives approaches previously published studies on 2D materials.[52–59]

In the presented work, we kept the same electrolyte for the entire electrochemical measurements to get clear insights into the material's intrinsic behaviour and preferred the CVT technique that yields high quality crystalline materials with the least defect density. From CV and GCD observations, it is also concluded that no functional groups were present at the surface of the electrode materials, so the exhibited electrochemical behaviour of our TMDC electrode materials can be decisively regarded as due to their intrinsic conductivity and layer spacings. In our synthesized electrode materials, the highest capacitance of TaS_2 can be dominantly attributed to its high conductivity, as substantiated with EIS and PDOS results, followed by ZrS_2, which although has slightly large interfacial resistance, on the other hand also possesses comparatively high inter-layer spacing. On the contrary, though the WSe_2 electrode keeps a small interface resistance value, it has moderate layer spacing which places it after TaS_2 and ZrS_2.

4 Conclusions

In summary, we have synthesized highly crystalline Ta-, W- and Zr-based 2H phase TMDCs using the chemical vapor transport technique and utilized them as an electrode material for electrochemical supercapacitors. The calculated specific capacitance values for the TaS_2, $TaSe_2$, WS_2, WSe_2, ZrS_2 and $ZrSe_2$ electrodes were 151.11, 102.6, 116.1, 152.3, 141.8 and 127.3 F cm^{-2} respectively. No functional groups were present on the surface of the electrode materials, and their capacitance values depend on the layer spacings and intrinsic conductivity. In the EIS results, it was observed that the WSe_2 electrode possessed the highest capacitance value followed by ZrS_2 up to around 500 Hz. On the contrary, the TaS_2 electrode encompasses comparable capacitance but holds it for a wide frequency range that is ~15 kHz. The high capacitance value of

the TaS_2 electrode was due to its high conductivity as revealed in the EIS analysis, which was further confirmed by the DFT calculations. Moreover, the supercapacitor behaviour was tested without using any type of conductive additive to confirm the intrinsic behaviour of the prepared crystalline TMDC electrode material. This study provides insights into the role of high interlayer spacing and intrinsic conductivity of the TMDC electrode materials in the field of electrochemical energy storage devices.

Conflicts of interest

There are no conflicts to declare.

Acknowledgements

We would like to thank our collaborators, the Prof. Song Li group from University of Science and Technology of China, for their support and facilitation of the work. This research was supported by the National Natural Science Foundation of China (Grant No. 62150410438).

References

1 H. Duan, G. Li, H. Tan, C. Wang, Q. Li, C. Liu, Y. Yin, X. Li, Z. Qi and W. Yan, Sulfur-vacancy-tunable interlayer magnetic coupling in centimeter-scale MoS_2 bilayer, *Nano Res.*, 2022, **15**, 881–888.

2 M. Habib, Z. Muhammad, R. Khan, C. Wu, Z. Ur Rehman, Y. Zhou, H. Liu and L. Song, Ferromagnetism in CVT grown tungsten diselenide single crystals with nickel doping, *Nanotechnology*, 2018, **29**(11), 115701.

3 S. Li, J. Hong, B. Gao, Y. C. Lin, H. E. Lim, X. Lu, J. Wu, S. Liu, Y. Tateyama and Y. Sakuma, Tunable Doping of Rhenium and Vanadium into Transition Metal Dichalcogenides for Two-Dimensional Electronics, *Adv. Sci.*, 2021, **8**(11), 2004438.

4 K. M. McCreary, M. Phillips, H.-J. Chuang, D. Wickramaratne, M. Rosenberger, C. S. Hellberg and B. T. Jonker, Stacking-dependent optical properties in bilayer WSe 2, *Nanoscale*, 2022, **14**(1), 147–156.

5 W. S. V. Lee, T. Xiong, X. Wang and J. Xue, Unraveling MoS_2 and transition metal dichalcogenides as functional zinc-ion battery cathode: A perspective, *Small Methods*, 2021, **5**(1), 2000815.

6 B. Li, Y. He, M. Xiao, Y. Zhang, Z. Wang, Z. Qin, B. Chai, J. Yan, J. Li and J. Li, A solar-light driven photocatalytic fuel cell for efficient electricity generation and organic wastewater degradation, *Colloids Surf., A*, 2022, **642**, 128205.

7 D. Vikraman, S. Hussain, K. Karuppasamy, A. Kathalingam, E.-B. Jo, A. Sanmugam, J. Jung and H.-S. Kim, Engineering the active sites tuned MoS_2 nanoarray structures by transition metal doping for hydrogen evolution and supercapacitor applications, *J. Alloys Compd.*, 2022, **893**, 162271.

8 S. Dutta and S. De, MoS_2 nanosheet/rGO hybrid: an electrode material for high performance thin film supercapacitor, *Mater. Today: Proc.*, 2018, **5**(3), 9771–9775.

9 G. Sun, J. Liu, X. Zhang, X. Wang, H. Li, Y. Yu, W. Huang, H. Zhang and P. Chen, Fabrication of ultralong hybrid microfibers from nanosheets of reduced graphene oxide and transition-metal dichalcogenides and their application as supercapacitors, *Angew. Chem., Int. Ed.*, 2014, **53**(46), 12576–12580.

10 S. Tanwar, N. Singh and A. Sharma, Structural and electrochemical performance of carbon coated molybdenum selenide nanocomposite for supercapacitor applications, *J. Energy Storage*, 2022, **45**, 103797.

11 D. Kesavan, V. K. Mariappan, P. Pazhamalai, K. Krishnamoorthy and S.-J. Kim, Topochemically synthesized MoS_2 nanosheets: a high performance electrode for wide-temperature tolerant aqueous supercapacitors, *J. Colloid Interface Sci.*, 2021, **584**, 714–722.

12 A. Chowdhury, S. Biswas, D. Mandal and A. Chandra, Facile strategy of using conductive additive supported $NaMnPO_4$ nanoparticles for delivering high performance Na-ion supercapacitors, *J. Alloys Compd.*, 2022, **902**, 163733.

13 S. Liu, C. Mao, Y. Niu, F. Yi, J. Hou, S. Lu, J. Jiang, M. Xu and C. Li, Facile synthesis of novel networked ultralong cobalt sulfide nanotubes and its application in supercapacitors, *ACS Appl. Mater. Interfaces*, 2015, **7**(46), 25568–25573.

14 Z.-Y. Zhao, W.-B. Zhang, X.-J. Ma, K. Li, Y. Zhao, J.-F. Gao, L. Kang and L.-B. Kong, A novel capacitive negative electrode material of Fe_3N, *Nano*, 2018, **13**(01), 1850002.

15 M. Canal-Rodríguez, J. A. Menéndez, M. A. Montes-Morán, I. Martín-Gullón, J. B. Parra and A. Arenillas, The role of conductive additives on the performance of hybrid carbon xerogels as electrodes in aqueous supercapacitors, *Electrochim. Acta*, 2019, **295**, 693–702.

16 N. Jäckel, D. Weingarth, A. Schreiber, B. Krüner, M. Zeiger, A. Tolosa, M. Aslan and V. Presser, Performance evaluation of conductive additives for activated carbon supercapacitors in organic electrolyte, *Electrochim. Acta*, 2016, **191**, 284–298.

17 R. Na, N. Lu, L. Li, Y. Liu, J. Luan, G. Wang and A. Robust, Conductive Polymer Network as a Multi-Functional Binder and Conductive Additive for Supercapacitors, *ChemElectroChem*, 2020, **7**(14), 3056–3064.

18 N. Guo, Y. Lin, Y. Cui, S. Su, H. Dai, J. Yang and X. Zhu, Effect of MWCNTs additive on preservation stability of rGO powder, *J. Mater. Sci.: Mater. Electron.*, 2022, **33**(9), 6766–6779.

19 Y. Niu, J. Wang, J. Zhang and Z. Shi, Graphene quantum dots as a novel conductive additive to improve the capacitive performance for supercapacitors, *J. Electroanal. Chem.*, 2018, **828**, 1–10.

20 J.-W. Wang, W.-K. Zhang, C. Jiao, F.-Y. Su, C.-M. Chen, C.-L. Guo, H. T. Chua and S. Eahon, Activated carbon based supercapacitors with a reduced graphene oxide additive: preparation and properties, *J. Nanosci. Nanotechnol.*, 2020, **20**(7), 4073–4083.

21 Z. Muhammad, Y. Wang, Y. Zhang, P. Vallobra, S. Peng, S. Yu, Z. Lv, H. Cheng and W. Zhao, Radiation-Tolerant Electronic Devices Using Wide Bandgap Semiconductors, *Adv. Mater. Technol.*, 2023, **8**(2), 2200539.

22 A. Khalil, Q. Liu, Q. He, T. Xiang, D. Liu, C. Wang, Q. Fang and L. Song, Metallic 1T-WS_2 nanoribbons as highly conductive electrodes for supercapacitors, *RSC Adv.*, 2016, **6**(54), 48788–48791.

23 Z. Liu, N. Li, C. Su, H. Zhao, L. Xu, Z. Yin, J. Li and Y. Du, Colloidal synthesis of 1T′ phase dominated WS_2 towards endurable electrocatalysis, *Nano Energy*, 2018, **50**, 176–181.

24 J. You, M. D. Hossain and Z. Luo, Synthesis of 2D transition metal dichalcogenides by chemical vapor deposition with controlled layer number and morphology, *Nano Convergence*, 2018, **5**, 1–13.

25 K. Ueno, Introduction to the growth of bulk single crystals of two-dimensional transition-metal dichalcogenides, *J. Phys. Soc. Jpn.*, 2015, **84**(12), 121015.

26 Z. Lin, B. R. Carvalho, E. Kahn, R. Lv, R. Rao, H. Terrones, M. A. Pimenta and M. Terrones, Defect engineering of two-dimensional transition metal dichalcogenides, *2D Mater.*, 2016, **3**(2), 022002.

27 Y. Sun, M. Terrones and R. E. Schaak, Colloidal nanostructures of transition-metal dichalcogenides, *Acc. Chem. Res.*, 2021, **54**(6), 1517–1527.

28 W. McMullan and J. Irwin, Long-wavelength phonons in 2H-NbS_2, 2H-TaS_2, and Ag_xTaS_2, *Can. J. Phys.*, 1984, **62**(8), 789–795.

29 M. Hangyo, S.-I. Nakashima and A. Mitsuishi, Raman spectroscopic studies of MX_2-type layered compounds, *Ferroelectrics*, 1983, **52**(1), 151–159.

30 X. Sun, *Optoelectronic Properties and Raman Spectra of Layered TaWSe$_2$ Ternary Alloys*, MSc (EE), Vanderbilt University, 2021.

31 X. Zhang, X.-F. Qiao, W. Shi, J.-B. Wu, D.-S. Jiang and P.-H. Tan, Phonon and Raman scattering of two-dimensional transition metal dichalcogenides from monolayer, multilayer to bulk material, *Chem. Soc. Rev.*, 2015, **44**(9), 2757–2785.

32 S. Mañas-Valero, V. García-López, A. Cantarero and M. Galbiati, Raman spectra of ZrS_2 and $ZrSe_2$ from bulk to atomically thin layers, *Appl. Sci.*, 2016, **6**(9), 264.

33 L. Roubi and C. Carlone, Resonance Raman spectrum of HfS_2 and ZrS_2, *Phys. Rev. B: Condens. Matter Mater. Phys.*, 1988, **37**(12), 6808.

34 X. Zhang, Q.-H. Tan, J.-B. Wu, W. Shi and P.-H. Tan, Review on the Raman spectroscopy of different types of layered materials, *Nanoscale*, 2016, **8**(12), 6435–6450.

35 M. Zhang, F. Heraly, M. Yi and J. Yuan, Multitasking tartaric-acid-enabled, highly conductive, and stable MXene/conducting polymer composite for ultrafast supercapacitor, *Cell Rep. Phys. Sci.*, 2021, **2**(6), 100449.

36 P. Sharma and T. Bhatti, A review on electrochemical double-layer capacitors, *Energy Convers. Manage.*, 2010, **51**(12), 2901–2912.

37 M. Winter and R. J. Brodd, What are batteries, fuel cells, and supercapacitors?, *Chem. Rev.*, 2004, **104**(10), 4245–4270.

38 M. Habib, A. Khalil, Z. Muhammad, R. Khan, C. Wang, Z. Ur Rehman, H. T. Masood, W. Xu, H. Liu and W. Gan, WX_2 (X = S, Se) single crystals: a highly stable material for supercapacitor applications, *Electrochim. Acta*, 2017, **258**, 71–79.

39 H. Li, H. Li, Z. Wu, L. Zhu, Y. Huang, X. Zhu and Y. Sun, Phase engineering of $Mo_{1-x}W_xS_2$ nanosheets for flexible supercapacitors, *Scr. Mater.*, 2022, **208**, 114346.

40 P. A. Basnayaka, M. K. Ram, L. Stefanakos and A. Kumar, Graphene/polypyrrole nanocomposite as electrochemical supercapacitor electrode: electrochemical impedance studies, *Graphene*, 2013, **2**(2), 81–87.

41 C. Wang, D. Liu, S. Chen, Y. Sang, Y. A. Haleem, C. Wu, W. Xu, Q. Fang, M. Habib and J. Cao, All-carbon ultrafast supercapacitor by integrating multidimensional nanocarbons, *Small*, 2016, **12**(41), 5684–5691.

42 R. Khan, M. Habib, M. A. Gondal, A. Khalil, Z. U. Rehman, Z. Muhammad, Y. A. Haleem, C. Wang, C. Q. Wu and L. Song, Facile synthesis of $CuFe_2O_4$–Fe_2O_3 composite for high-performance supercapacitor electrode applications, *Mater. Res. Express*, 2017, **4**(10), 105501.

43 P. Taberna, P. Simon and J.-F. Fauvarque, Electrochemical characteristics and impedance spectroscopy studies of carbon-carbon supercapacitors, *J. Electrochem. Soc.*, 2003, **150**(3), A292.

44 L. Cao, S. Yang, W. Gao, Z. Liu, Y. Gong, L. Ma, G. Shi, S. Lei, Y. Zhang and S. Zhang, Direct laser-patterned micro-supercapacitors from paintable MoS_2 films, *Small*, 2013, **9**(17), 2905–2910.

45 A. Winchester, S. Ghosh, S. Feng, A. L. Elias, T. Mallouk, M. Terrones and S. Talapatra, Electrochemical characterization of liquid phase exfoliated two-dimensional layers of molybdenum disulfide, *ACS Appl. Mater. Interfaces*, 2014, **6**(3), 2125–2130.

46 P. Zhu, Y. Wang, M. Zhang, Y. Wu and W. Cai, Anions influence on the electrochemical performance of Co_3X_4 (X = O, Se) for supercapacitor: Experiments and theoretical calculations, *Appl. Surf. Sci.*, 2022, **574**, 151646.

47 L. Zhang, F. Zhang, X. Yang, G. Long, Y. Wu, T. Zhang, K. Leng, Y. Huang, Y. Ma and A. Yu, Porous 3D graphene-based bulk materials with exceptional high surface area and excellent conductivity for supercapacitors, *Sci. Rep.*, 2013, **3**(1), 1408.

48 M. Acerce, D. Voiry and M. Chhowalla, Metallic 1T phase MoS_2 nanosheets as supercapacitor electrode materials, *Nat. Nanotechnol.*, 2015, **10**(4), 313–318.

49 K. O. Oyedotun, T. M. Masikhwa, S. Lindberg, A. Matic, P. Johansson and N. Manyala, Comparison of ionic liquid electrolyte to aqueous electrolytes on carbon nanofibres supercapacitor electrode derived from oxygen-functionalized graphene, *Chem. Eng. J.*, 2019, **375**, 121906.

50 F. Zhang, T.-Y. Eom, M. Cho, H.-J. Lee and H. Pang, Fabrication of defect-rich bifunctional hollow $NiTe_2$ nanotubes for high performance hydrogen evolution electrocatalysts and supercapacitors, *J. Energy Storage*, 2021, **42**, 103098.

51 X. Han, Z.-H. Huang, F. Meng, B. Jia and T. Ma, Redox-etching induced porous carbon cloth with pseudocapacitive oxygenic groups for flexible symmetric supercapacitor, *J. Energy Chem.*, 2022, **64**, 136–143.

52 R. B. Rakhi, B. Ahmed, M. N. Hedhili, D. H. Anjum and H. N. Alshareef, Effect of postetch annealing gas

composition on the structural and electrochemical properties of Ti_2CT_x MXene electrodes for supercapacitor applications, *Chem. Mater.*, 2015, **27**(15), 5314–5323.

53 M. Cao, F. Wang, L. Wang, W. Wu, W. Lv and J. Zhu, Room temperature oxidation of Ti_3C_2 MXene for supercapacitor electrodes, *J. Electrochem. Soc.*, 2017, **164**(14), A3933.

54 A. Zaheer, S. A. Zahra, M. Z. Iqbal, A. Mahmood, S. A. Khan and S. Rizwan, Nickel-adsorbed two-dimensional Nb_2C MXene for enhanced energy storage applications, *RSC Adv.*, 2022, **12**(8), 4624–4634.

55 Y. Guan, S. Jiang, Y. Cong, J. Wang, Z. Dong and Q. Zhang, *et al.*, A hydrofluoric acid-free synthesis of 2D vanadium carbide (V_2C) MXene for supercapacitor electrodes, *2D Mater.*, 2020, **7**(2), 025010.

56 S. Venkateshalu, J. Cherusseri, M. Karnan, K. S. Kumar, P. Kollu and M. Sathish, *et al.*, New method for the synthesis of 2D vanadium nitride (MXene) and its application as a supercapacitor electrode, *ACS Omega*, 2020, **5**(29), 17983–17992.

57 H. Gupta, S. Chakrabarti, S. Mothkuri, B. Padya, T. Rao and P. Jain, High performance supercapacitor based on 2D-MoS_2 nanostructures, *Mater. Today: Proc.*, 2020, **26**, 20–24.

58 S. Mothkuri, S. Chakrabarti, H. Gupta, B. Padya, T. Rao and P. Jain, Synthesis of MnO_2 nano-flakes for high performance supercapacitor application, *Mater. Today: Proc.*, 2020, **26**, 142–147.

59 T. Purkait, G. Singh, D. Kumar, M. Singh and R. S. Dey, High-performance flexible supercapacitors based on electrochemically tailored three-dimensional reduced graphene oxide networks, *Sci. Rep.*, 2018, **8**(1), 640.